Modular Multilevel Converter With Magnetically Coupled Branch Inductors

Jakub Kucka, *Student Member, IEEE*, Dennis Karwatzki, *Student Member, IEEE*, Lennart Baruschka, *Member, IEEE*, and Axel Mertens, *Member, IEEE*

***Abstract*—The modular multilevel converter is a well-known modular multilevel topology. This paper proposes a novel branch inductor coupling and compares it to the center-tapped inductor and the standard noncoupled inductor topology. The proposed coupling has a significant influence on the inductor and converter dimensioning. Its properties make it especially well suited for use in single-to-three-phase ac/ac modular multilevel converter applications.**

***Index Terms*—Branch inductor, inductor coupling, modular multilevel converter (M^2LC).**

I. Introduction

MODULAR multilevel converter topologies have already been in the focus of scientific investigation for several years. Their main advantages such as their simple scalability, redundancy, and low harmonic distortion make them a good choice for medium- and high-voltage high-power drives and conversion systems.

The topology family originates from the cascaded H-bridge converter with isolating transformer [2]. The disadvantage of the advanced isolating transformer requirement was solved later with the modular multilevel converter (M^2LC)—first described by Marquardt *et al.* in 2002 [3]—for which a novel coupled branch inductor will be presented in this paper. More recently, the direct ac/ac converters modular multilevel matrix converter (MMMC) [4] and Hexverter [5] were presented. These topologies were also improved by coupling the branch inductors (MMMC [6], [7] and Hexverter [8]).

The idea of coupled branch inductors for the M^2LC is not completely new. A coupling of the inductors, preventing the branch inductors from influencing the three-phase output currents, has already been presented as a center-tapped inductor [9], [10]. This configuration will also be compared with the proposed coupling

Since the invention of the M^2LC, different control strategies have been derived. The decoupled control of the input, output, and circulating currents shows some significant advantages and will be used for the design verification. To reduce the branch energy variation at low output frequencies, the so-called low frequency mode was described by Korn *et al.* [11].

The M^2LC is usually presented as a half-bridge dc/ac converter. In this paper, the single-to-three-phase ac/ac H-bridge version (ACM^2LC), described in [12]–[15], will also be taken into consideration.

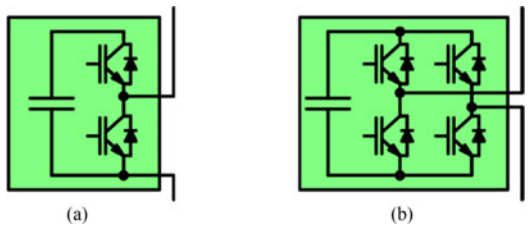

Fig. 1. Module schematics. (a) Half-bridge module. (b) H-bridge module.

II. M^2LC Description and Equation System

The M^2LC is a converter consisting of six modular branches, Fig. 2(a). Each branch consists of several generic modules and one inductor. If the voltage on side 1 v_1 (referred to as input voltage) is assumed to be a direct voltage, the modules are usually constructed as half-bridge modules, Fig. 1(a). In the case of an ACM^2LC, the modules are to be constructed as H-bridge modules, Fig. 1(b).

In this section, a state-space description will be used for comparing the particular inductor topologies. The effects of different couplings on the converter's behaviour can be recognized by observing the state-space matrices. Using these matrices, the values of the effective inductances affecting the particular currents will be derived in Section III. Besides, the input matrix $\mathbf{B}$ can be used as a basis for decoupled current control [16], [17]. To derive the system of state-space equations, an equivalent electrical circuit, as depicted in Fig. 2(b), is used. The equation system remains unchanged when using an ACM^2LC, as it is represented by the same equivalent electrical circuit. When using the amplitude-invariant $\alpha, \beta, 0$-transformation on side 2

Manuscript received May 6, 2016; revised July 18, 2016 and September 29, 2016; accepted October 27, 2016. Date of publication November 10, 2016; date of current version April 24, 2017. This paper was presented in part at the *7th Annual IEEE Energy Conversion Congress and Exposition*, Montreal, QC, Canada, September 2015. Recommended for publication by Associate Editor Marcelo A. Perez.

J. Kucka, D. Karwatzki and A. Mertens are with the Institute for Drive Systems and Power Electronics, Leibniz Universität Hannover, Hannover 30167, Germany (e-mail: jakub.kucka@ial.uni-hannover.de; dennis.karwatzki@ial.uni-hannover.de; mertens@ial.uni-hannover.de).

L. Baruschka is with Protolar GmbH, Hannover 30419, Germany (e-mail: baruschka@protolar.de).

Color versions of one or more of the figures in this paper are available online at http://ieeexplore.ieee.org.

Digital Object Identifier 10.1109/TPEL.2016.2627882

See http://www.ieee.org/publications_standards/publications/rights/index.html for more information.

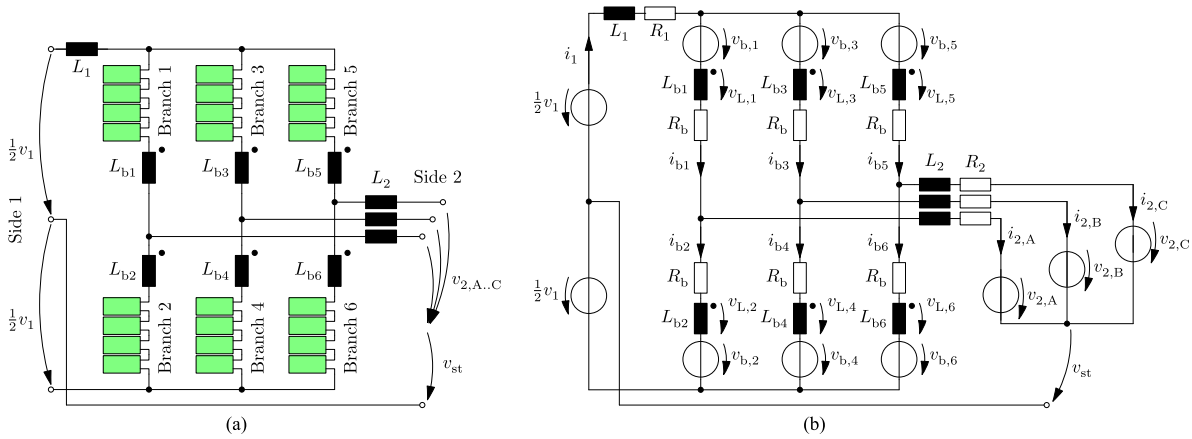

Fig. 2. M^{2}LC. (a) Topology schematic. (b) Equivalent electrical circuit.

variables, the system is described as

$$\frac{\partial}{\partial t}\begin{bmatrix} i_1 \\ i_{2,\alpha} \\ i_{2,\beta} \\ i_{\mathrm{cir},1} \\ i_{\mathrm{cir},2} \end{bmatrix} = \mathbf{A}\cdot\begin{bmatrix} i_1 \\ i_{2,\alpha} \\ i_{2,\beta} \\ i_{\mathrm{cir},1} \\ i_{\mathrm{cir},2} \end{bmatrix} + \mathbf{B}\cdot\begin{bmatrix} v_{\mathrm{b},1} \\ v_{\mathrm{b},2} \\ v_{\mathrm{b},3} \\ v_{\mathrm{b},4} \\ v_{\mathrm{b},5} \\ v_{\mathrm{b},6} \end{bmatrix} + \mathbf{E}\cdot\begin{bmatrix} v_1 \\ v_{2,\alpha} \\ v_{2,\beta} \\ v_{2,0} \end{bmatrix} \quad (1)$$

with the star-point voltage

$$v_{\mathrm{st}} = \frac{1}{6}\cdot(-v_{\mathrm{b},1} + v_{\mathrm{b},2} - v_{\mathrm{b},3} + v_{\mathrm{b},4} - v_{\mathrm{b},5} + v_{\mathrm{b},6}). \quad (2)$$

The circulating currents $i_{\mathrm{cir},1}$ and $i_{\mathrm{cir},2}$ are two internal currents circulating only through the modules. They may be chosen in different ways, here

$$\begin{bmatrix} i_{\mathrm{cir},1} \\ i_{\mathrm{cir},2} \end{bmatrix} = \frac{1}{4}\begin{bmatrix} i_{\mathrm{b},1} + i_{\mathrm{b},2} - i_{\mathrm{b},3} - i_{\mathrm{b},4} \\ i_{\mathrm{b},3} + i_{\mathrm{b},4} - i_{\mathrm{b},5} - i_{\mathrm{b},6} \end{bmatrix} \quad (3)$$

is used.

Considering the number of winding turns w and the magnetic reluctance $\mathcal{R}$ while using Hopkinson's Law and superposition, the part of the magnetic flux ϕ_x, which is caused by a particular winding x, can be defined as

$$\phi_x = \frac{w}{\mathcal{R}}\cdot i_{\mathrm{b},x}. \quad (4)$$

A. Simple Noncoupled Inductors

At first, the equation system with noncoupled inductors is analyzed. The inductor voltage $v_{L,x}$ at branch x (Fig. 2(b)) is described as

$$v_{L,x} = w\cdot\frac{\partial}{\partial t}\phi_x = \frac{w^2}{\mathcal{R}}\cdot\frac{\partial}{\partial t}i_{\mathrm{b},x}, x = 1..6. \quad (5)$$

Simplifying this inductor voltage using the substitution (6), the equation system resulting from Fig. 2(b) can be solved, resulting in the matrices $\mathbf{A}_{\mathrm{NC}}$, $\mathbf{B}_{\mathrm{NC}}$, and $\mathbf{E}_{\mathrm{NC}}$, displayed in Table I. Index "NC" refers to the topology with noncoupled inductors.

For clarity reasons, the following substitution is applied in the state-space matrices:

$$L_{\mathrm{b}} = \frac{w^2}{\mathcal{R}}. \quad (6)$$

B. Center-Tapped Inductors

The center-tapped inductors were presented in [9] and [10], and their principle is displayed in Fig. 3. The main idea of this coupling is to construct the inductors in a way that they do not affect the three-phase currents on side 2.

Using the fluxes ϕ_{A}, ϕ_{B}, and ϕ_{C}

$$\begin{bmatrix} \phi_{\mathrm{A}} \\ \phi_{\mathrm{B}} \\ \phi_{\mathrm{C}} \end{bmatrix} = \begin{bmatrix} 1 & 1 & 0 & 0 & 0 & 0 \\ 0 & 0 & 1 & 1 & 0 & 0 \\ 0 & 0 & 0 & 0 & 1 & 1 \end{bmatrix}\cdot\begin{bmatrix} \phi_1 \\ \phi_2 \\ \phi_3 \\ \phi_4 \\ \phi_5 \\ \phi_6 \end{bmatrix} \quad (7)$$

the voltage at the particular inductors can be obtained by

$$\begin{bmatrix} v_{L,1} \\ v_{L,3} \\ v_{L,5} \end{bmatrix} = \begin{bmatrix} v_{L,2} \\ v_{L,4} \\ v_{L,6} \end{bmatrix} = w\cdot\frac{\partial}{\partial t}\begin{bmatrix} \phi_{\mathrm{A}} \\ \phi_{\mathrm{B}} \\ \phi_{\mathrm{C}} \end{bmatrix} = \frac{w^2}{\mathcal{R}}\cdot\frac{\partial}{\partial t}\begin{bmatrix} i_{\mathrm{b},1} + i_{\mathrm{b},2} \\ i_{\mathrm{b},3} + i_{\mathrm{b},4} \\ i_{\mathrm{b},5} + i_{\mathrm{b},6} \end{bmatrix}. \quad (8)$$

Solving the voltage equation system results in the state-space representation matrices $\mathbf{A}_{\mathrm{CT}}$, $\mathbf{B}_{\mathrm{CT}}$, and $\mathbf{E}_{\mathrm{CT}}$, Table I. The center-tapped M^{2}LC topology is denoted by the index "CT".

C. Proposed Inductor Coupling

The main idea of the proposed coupling, displayed in Fig. 4, is to exclude an influence of the branch inductors on the input and output currents and vice versa.

In this case, the fluxes ϕ_{A}, ϕ_{B}, and ϕ_{C} are influenced by all of the partial fluxes

$$\begin{bmatrix} \phi_{\mathrm{A}} \\ \phi_{\mathrm{B}} \\ \phi_{\mathrm{C}} \end{bmatrix} = \begin{bmatrix} 1 & 1 & -\frac{1}{2} & -\frac{1}{2} & -\frac{1}{2} & -\frac{1}{2} \\ -\frac{1}{2} & -\frac{1}{2} & 1 & 1 & -\frac{1}{2} & -\frac{1}{2} \\ -\frac{1}{2} & -\frac{1}{2} & -\frac{1}{2} & -\frac{1}{2} & 1 & 1 \end{bmatrix}\cdot\begin{bmatrix} \phi_1 \\ \phi_2 \\ \phi_3 \\ \phi_4 \\ \phi_5 \\ \phi_6 \end{bmatrix}. \quad (9)$$

TABLE I
STATE-SPACE REPRESENTATION MATRICES FOR DIFFERENT INDUCTOR COUPLINGS

noncoupled

$$\mathbf{A}_{\mathrm{NC}} = \begin{bmatrix} -\frac{3R_1+2R_\mathrm{b}}{3L_1+2L_\mathrm{b}} & 0 & 0 & 0 & 0 \\ 0 & -\frac{2R_2+R_\mathrm{b}}{2L_2+L_\mathrm{b}} & 0 & 0 & 0 \\ 0 & 0 & -\frac{2R_2+R_\mathrm{b}}{2L_2+L_\mathrm{b}} & 0 & 0 \\ 0 & 0 & 0 & -\frac{R_\mathrm{b}}{L_\mathrm{b}} & 0 \\ 0 & 0 & 0 & 0 & -\frac{R_\mathrm{b}}{L_\mathrm{b}} \end{bmatrix}, \mathbf{E}_{\mathrm{NC}} = \begin{bmatrix} \frac{3}{3L_1+2L_\mathrm{b}} & 0 & 0 & 0 \\ 0 & -\frac{2}{2L_2+L_\mathrm{b}} & 0 & 0 \\ 0 & 0 & -\frac{2}{2L_2+L_\mathrm{b}} & 0 \\ 0 & 0 & 0 & 0 \\ 0 & 0 & 0 & 0 \end{bmatrix},$$

$$\mathbf{B}_{\mathrm{NC}} = \begin{bmatrix} -\frac{1}{3L_1+2L_\mathrm{b}} & -\frac{1}{3L_1+2L_\mathrm{b}} & -\frac{1}{3L_1+2L_\mathrm{b}} & -\frac{1}{3L_1+2L_\mathrm{b}} & -\frac{1}{3L_1+2L_\mathrm{b}} & -\frac{1}{3L_1+2L_\mathrm{b}} \\ -\frac{2}{6L_2+3L_\mathrm{b}} & \frac{2}{6L_2+3L_\mathrm{b}} & \frac{1}{6L_2+3L_\mathrm{b}} & -\frac{1}{6L_2+3L_\mathrm{b}} & \frac{1}{6L_2+3L_\mathrm{b}} & -\frac{1}{6L_2+3L_\mathrm{b}} \\ 0 & 0 & -\frac{\sqrt{3}}{6L_2+3L_\mathrm{b}} & \frac{\sqrt{3}}{6L_2+3L_\mathrm{b}} & \frac{\sqrt{3}}{6L_2+3L_\mathrm{b}} & -\frac{\sqrt{3}}{6L_2+3L_\mathrm{b}} \\ -\frac{1}{4L_\mathrm{b}} & -\frac{1}{4L_\mathrm{b}} & \frac{1}{4L_\mathrm{b}} & \frac{1}{4L_\mathrm{b}} & 0 & 0 \\ 0 & 0 & -\frac{1}{4L_\mathrm{b}} & -\frac{1}{4L_\mathrm{b}} & \frac{1}{4L_\mathrm{b}} & \frac{1}{4L_\mathrm{b}} \end{bmatrix}.$$

center-tapped

$$\mathbf{A}_{\mathrm{CT}} = \begin{bmatrix} -\frac{3R_1+2R_\mathrm{b}}{3L_1+4L_\mathrm{b}} & 0 & 0 & 0 & 0 \\ 0 & -\frac{2R_2+R_\mathrm{b}}{2L_2} & 0 & 0 & 0 \\ 0 & 0 & -\frac{2R_2+R_\mathrm{b}}{2L_2} & 0 & 0 \\ 0 & 0 & 0 & -\frac{R_\mathrm{b}}{2L_\mathrm{b}} & 0 \\ 0 & 0 & 0 & 0 & -\frac{R_\mathrm{b}}{2L_\mathrm{b}} \end{bmatrix}, \mathbf{E}_{\mathrm{CT}} = \begin{bmatrix} \frac{3}{3L_1+4L_\mathrm{b}} & 0 & 0 & 0 \\ 0 & -\frac{1}{L_2} & 0 & 0 \\ 0 & 0 & -\frac{1}{L_2} & 0 \\ 0 & 0 & 0 & 0 \\ 0 & 0 & 0 & 0 \end{bmatrix},$$

$$\mathbf{B}_{\mathrm{CT}} = \begin{bmatrix} -\frac{1}{3L_1+4L_\mathrm{b}} & -\frac{1}{3L_1+4L_\mathrm{b}} & -\frac{1}{3L_1+4L_\mathrm{b}} & -\frac{1}{3L_1+4L_\mathrm{b}} & -\frac{1}{3L_1+4L_\mathrm{b}} & -\frac{1}{3L_1+4L_\mathrm{b}} \\ -\frac{1}{3L_2} & \frac{1}{3L_2} & \frac{1}{6L_2} & -\frac{1}{6L_2} & \frac{1}{6L_2} & -\frac{1}{6L_2} \\ 0 & 0 & -\frac{\sqrt{3}}{6L_2} & \frac{\sqrt{3}}{6L_2} & \frac{\sqrt{3}}{6L_2} & -\frac{\sqrt{3}}{6L_2} \\ -\frac{1}{8L_\mathrm{b}} & -\frac{1}{8L_\mathrm{b}} & \frac{1}{8L_\mathrm{b}} & \frac{1}{8L_\mathrm{b}} & 0 & 0 \\ 0 & 0 & -\frac{1}{8L_\mathrm{b}} & -\frac{1}{8L_\mathrm{b}} & \frac{1}{8L_\mathrm{b}} & \frac{1}{8L_\mathrm{b}} \end{bmatrix}.$$

proposed

$$\mathbf{A}_{\mathrm{P}} = \begin{bmatrix} -\frac{3R_1+2R_\mathrm{b}}{3L_1} & 0 & 0 & 0 & 0 \\ 0 & -\frac{2R_2+R_\mathrm{b}}{2L_2} & 0 & 0 & 0 \\ 0 & 0 & -\frac{2R_2+R_\mathrm{b}}{2L_2} & 0 & 0 \\ 0 & 0 & 0 & -\frac{R_\mathrm{b}}{3L_\mathrm{b}} & 0 \\ 0 & 0 & 0 & 0 & -\frac{R_\mathrm{b}}{3L_\mathrm{b}} \end{bmatrix}, \mathbf{E}_{\mathrm{P}} = \begin{bmatrix} \frac{1}{L_1} & 0 & 0 & 0 \\ 0 & -\frac{1}{L_2} & 0 & 0 \\ 0 & 0 & -\frac{1}{L_2} & 0 \\ 0 & 0 & 0 & 0 \\ 0 & 0 & 0 & 0 \end{bmatrix},$$

$$\mathbf{B}_{\mathrm{P}} = \begin{bmatrix} -\frac{1}{3L_1} & -\frac{1}{3L_1} & -\frac{1}{3L_1} & -\frac{1}{3L_1} & -\frac{1}{3L_1} & -\frac{1}{3L_1} \\ -\frac{1}{3L_2} & \frac{1}{3L_2} & \frac{1}{6L_2} & -\frac{1}{6L_2} & \frac{1}{6L_2} & -\frac{1}{6L_2} \\ 0 & 0 & -\frac{\sqrt{3}}{6L_2} & \frac{\sqrt{3}}{6L_2} & \frac{\sqrt{3}}{6L_2} & -\frac{\sqrt{3}}{6L_2} \\ -\frac{1}{12L_\mathrm{b}} & -\frac{1}{12L_\mathrm{b}} & \frac{1}{12L_\mathrm{b}} & \frac{1}{12L_\mathrm{b}} & 0 & 0 \\ 0 & 0 & -\frac{1}{12L_\mathrm{b}} & -\frac{1}{12L_\mathrm{b}} & \frac{1}{12L_\mathrm{b}} & \frac{1}{12L_\mathrm{b}} \end{bmatrix}.$$

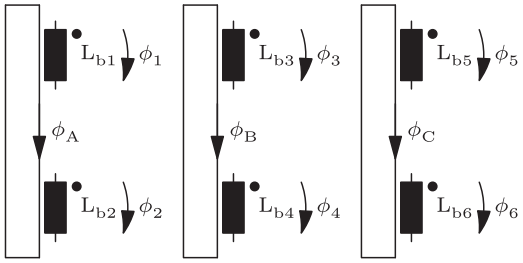

Fig. 3. Simplified representation of center-tapped inductor coupling.

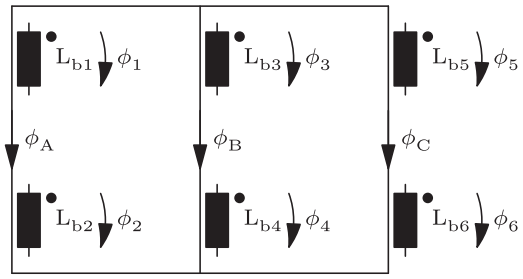

Fig. 4. Simplified representation of the proposed inductor coupling.

The voltage at the particular windings can be written as

$$\begin{bmatrix} v_{L,1} \\ v_{L,3} \\ v_{L,5} \end{bmatrix} = \begin{bmatrix} v_{L,2} \\ v_{L,4} \\ v_{L,6} \end{bmatrix} = w \cdot \frac{\partial}{\partial t} \begin{bmatrix} \phi_{\mathrm{A}} \\ \phi_{\mathrm{B}} \\ \phi_{\mathrm{C}} \end{bmatrix} = \frac{w^2}{\mathcal{R}} \cdot$$

$$\frac{\partial}{\partial t} \begin{bmatrix} i_{\mathrm{b},1} + i_{\mathrm{b},2} - \frac{1}{2} i_{\mathrm{b},3} - \frac{1}{2} i_{\mathrm{b},4} - \frac{1}{2} i_{\mathrm{b},5} - \frac{1}{2} i_{\mathrm{b},6} \\ i_{\mathrm{b},3} + i_{\mathrm{b},4} - \frac{1}{2} i_{\mathrm{b},1} - \frac{1}{2} i_{\mathrm{b},2} - \frac{1}{2} i_{\mathrm{b},5} - \frac{1}{2} i_{\mathrm{b},6} \\ i_{\mathrm{b},5} + i_{\mathrm{b},6} - \frac{1}{2} i_{\mathrm{b},1} - \frac{1}{2} i_{\mathrm{b},2} - \frac{1}{2} i_{\mathrm{b},3} - \frac{1}{2} i_{\mathrm{b},4} \end{bmatrix} \quad (10)$$

which leads to the matrices $\mathbf{A}_{\mathrm{P}}$, $\mathbf{B}_{\mathrm{P}}$, and $\mathbf{E}_{\mathrm{P}}$, given in Table I. Index "P" refers to the proposed topology.

III. General Considerations for Dimensioning

The first significant changes caused by the branch inductor coupling are visible at the disturbance matrix $\mathbf{E}$ showing the effective inductance applied to the input and output currents. The value of the effective inductance for circulating currents can be derived from the system matrices $\mathbf{A}$ for the particular topologies. The values of the effective inductances affecting the particular currents are shown in Table II.

These inductances are important to suppress the current ripple. Their values are mainly chosen as a tradeoff between maximum current ripple and price. For a fixed value of circulating-current inductance, the dimensioning of the proposed inductors leads to a cost benefit. For the same value of $\mathcal{R}$, $\sqrt{3}$ times less winding turns are required in comparison to standard inductors, and $\sqrt{1.5}$ less compared with center-tapped inductors. Accordingly, this leads to a lower winding resistance, improving the efficiency of the inductor. Since the input and output currents do not affect the core material, it has to be designed only for the circulating currents. For the standard operation of the M^{2}LC, the circulating currents are much lower than the input and output currents. The cross-sectional area can, therefore, be smaller, allowing for significant savings of the core material.

TABLE II
Effective Inductance Values Applied to the Particular Currents

Current	Standard	Center tapped	Proposed
Input current	$L_1 + \frac{2}{3}\frac{w^2}{\mathcal{R}}$	$L_1 + \frac{4}{3}\frac{w^2}{\mathcal{R}}$	L_1
Output currents	$L_2 + \frac{1}{2}\frac{w^2}{\mathcal{R}}$	L_2	L_2
Circulating currents	$4\frac{w^2}{\mathcal{R}}$	$8\frac{w^2}{\mathcal{R}}$	$12\frac{w^2}{\mathcal{R}}$

A higher value of the effective inductance leads to a lower current distortion. However, the higher value also means a higher value of the voltage drop over these inductances, resulting in a higher maximum branch voltage, i.e., a larger number of necessary modules. The value of the branch inductance can be chosen freely; on the other hand, the values of the input and output inductances are often dependent on the characteristics of the systems the converter is connected to. As visible in Table II, the center-tapped inductor system lowers the effective inductance on side 2. This makes it advantageous for an M^{2}LC drive system, in which the load inductance L_2 is mostly significantly higher than the part delivered by the noncoupled branch inductor. Therefore, the total current distortion is affected only minorly. If the effective inductances can be lowered on both sides, because the inductances L_1 and L_2 given by the systems are sufficient (e.g., with an ACM^{2}LC drive with a transformer on side 1), the proposed inductor configuration is more advantageous.

IV. Inductor Geometry Calculation

As mentioned, the main task of the inductor is to suppress the current ripple. If the inductance at the connected systems is sufficient, only the effective inductance applied to the circulating currents has to be considered. The geometry dimensions (Fig. 5) and number of turns are chosen to fit the following constraints.

1) The inductor must not come into saturation; therefore, the magnetic field in the core must not exceed the value $B_{\max}$ (assumed to be 1 T). This defines the maximum magnetic flux in the core $\phi_{\max} = A_{\mathrm{c}} \cdot B_{\max}$. It is assumed that the cross-sectional area A_{c} is a square with a side length of a.
2) The cross-sectional area of the winding wire is determined by the maximum current density $J_{\max}$ (here, 3 A/mm^2). The area of the window needed for the winding $A_{\mathrm{w}} = i_{\mathrm{b,max}}/(J_{\max} \cdot k_w)$ is assumed to be a square with a side length of b. The window utilization factor k_w takes into account the space needed for insulation, and the efficiency of the winding process and is assumed to be 0.4.
3) The permeability of the core is significantly higher than air permeability, therefore, the magnetic reluctance of the core can be neglected.

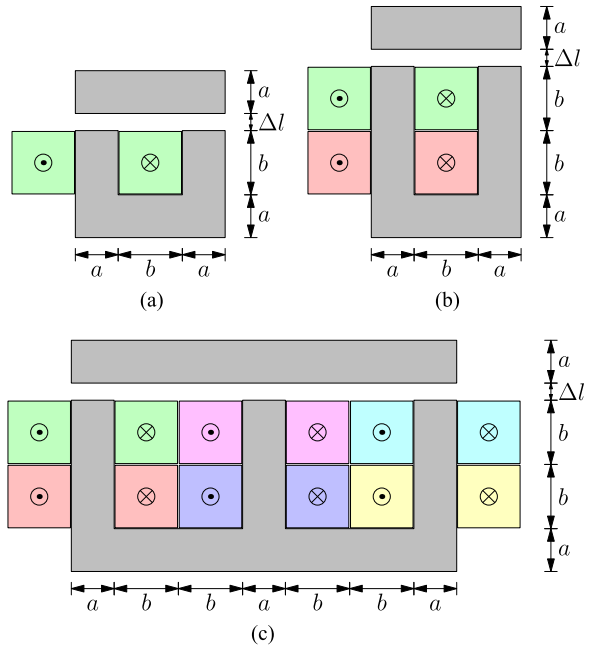

Fig. 5. Outline drawings of discussed inductors; the colors represent separate windings; the position of the particular windings is according to Figs. 3 and 4. (a) Noncoupled. (b) Center tapped. (c) Proposed.

4) The length of one turn for branch inductor resistance (R_b) calculation is approximated with $l_{1\mathrm{w}} = 4 \cdot (a + b)$, and the copper resistivity is 17.1 nΩ·m.

The effective inductance applied to the circulating currents L_cir, the magnetic reluctance for a particular inductor $\mathcal{R}$, and the maximum magnetic flux ϕ_max are determined differently for each topology.

A. Noncoupled Inductor Topology

The chosen circulating-current inductance

$$L_\mathrm{cir} = 4 \cdot \frac{w_\mathrm{NC}^2}{\mathcal{R}_\mathrm{NC}} \tag{11}$$

is determined (according to Table II) by the number of turns w_NC and the magnetic reluctance for this topology

$$\mathcal{R}_\mathrm{NC} = \frac{2 \cdot \Delta l}{\mu_0 \cdot A_\mathrm{c}} \quad . \tag{12}$$

The maximum magnetic flux in the core

$$\phi_\mathrm{NC,max} = \frac{w_\mathrm{NC} \cdot i_\mathrm{b,max}}{\mathcal{R}_\mathrm{NC}} \tag{13}$$

is dependent on the maximum branch current $i_\mathrm{b,max}$.

B. Center-Tapped Inductor Topology

The circulating-current inductance for the center-tapped topology is determined as

$$L_\mathrm{cir} = 8 \cdot \frac{w_\mathrm{CT}^2}{\mathcal{R}_\mathrm{CT}} \quad . \tag{14}$$

The magnetic reluctance for this case is calculated equally to the noncoupled topology: $\mathcal{R}_\mathrm{CT} = \mathcal{R}_\mathrm{NC}$. The maximum magnetic flux in the core

$$\phi_\mathrm{CT,max} = \frac{w_\mathrm{CT} \cdot 2 \cdot (\frac{1}{3} \cdot i_\mathrm{1,max} + \frac{4}{3} \cdot i_\mathrm{cir,max})}{\mathcal{R}_\mathrm{CT}} \tag{15}$$

results from the superposition of the maximum values of current on side 1 $i_\mathrm{1,max}$ (of which $\frac{1}{3}$ flows in each branch) and the maximum of circulating currents $i_\mathrm{cir,max}$.

C. Proposed Topology

The circulating-current inductance for the proposed topology is determined as

$$L_\mathrm{cir} = 12 \cdot \frac{w_\mathrm{P}^2}{\mathcal{R}_\mathrm{P}} \quad . \tag{16}$$

The magnetic reluctance

$$\mathcal{R}_\mathrm{P} = \frac{\frac{3}{2} \cdot \Delta l}{\mu_0 \cdot A_\mathrm{c}} \tag{17}$$

can be obtained from Hopkinson's law. The maximum magnetic flux in the core

$$\phi_\mathrm{P,max} = \frac{w_\mathrm{P} \cdot (4 \cdot i_\mathrm{cir,max})}{\mathcal{R}_\mathrm{P}} \tag{18}$$

results only from the superposition of the maximum circulating currents.

V. Dimensioning Comparison

The dimensioning will be compared for three standard cases where an M^{2}LC could be used. The inductance on side 1 and 2 is assumed to be sufficient for the converter operation also with the proposed topology. The simplified calculation from Section IV is applied to make the results generally scalable to other power classes. Note that for a meaningful economical comparison, the commercial availability of the inductor cores must also be considered.

Case A: M^{2}LC Without Low-Frequency Mode

This case usually appears when either the frequency on side 2 is constant (e.g., active front end) or the power rises overproportionally to this frequency (e.g., wind power plants and compressor drives). Without the low-frequency mode, the circulating currents are significantly lower in comparison to the branch currents, as they are used only to compensate asymmetries in the system.

For the dimensioning example, the measured data from 10 kW H-bridge module M^{2}LC from [18] were used. In this application, the M^{2}LC is connected to a 50 Hz grid and the switching frequency of the two modules is 2 kHz each, resulting in an apparent switching frequency of the output voltages (and currents) of 4 kHz. According to the paper, the effective inductance for the circulating current is $L_\mathrm{cir} = 2$ mH. The maximum branch current $i_\mathrm{b,max} = 40$ A, the maximum side-1 current $i_\mathrm{1,max} = 36$ A, and the maximum circulating current $i_\mathrm{cir,max} = 2.5$ A can be stated after transforming the currents from [18, Fig. 13] to the definition of currents given above.

In Table III, the dimensioning results are listed. The proposed topology shows significantly lower material requirements when

TABLE III
INDUCTOR DESIGN RESULTS FOR CASE A EXAMPLE

	Noncoupled	Center tapped	Proposed
w	24	16	10
a	2.89 cm	2.19 cm	1.29 cm
b	2.83 cm	2.31 cm	1.83 cm
Δl	0.6 mm	0.31 mm	0.08 mm
R_{b}	7 mΩ	3.67 mΩ	1.59 mΩ
Total copper volume	0.44 ℓ	0.23 ℓ	0.1 ℓ
Total core volume	1.14 ℓ	0.33 ℓ	0.07 ℓ

TABLE IV
INDUCTOR DESIGN RESULTS FOR CASE B EXAMPLE

	Noncoupled	Center tapped	Proposed
w	24	16	14
a	2.68 cm	2.28 cm	2.18 cm
b	2.62 cm	2.14 cm	2 cm
Δl	0.52 mm	0.33 mm	0.47 mm
R_{b}	7.54 mΩ	4.19 mΩ	3.47 mΩ
Total copper volume	0.35 ℓ	0.19 ℓ	0.16 ℓ
Total core volume	0.91 ℓ	0.34 ℓ	0.23 ℓ

compared with the others. This is caused by a relatively low circulating current, from which the maximum flux at the core is determined. Moreover, the dimensioning is even expected to be superior, if an additional inductor on side 1 is required (with the same geometry as the noncoupled inductor and 24 winding turns, additional 0.06 ℓ of copper and 0.1 ℓ of core are needed). However, please note that the benefit of the proposed topology is determined by the maximum allowable circulating current.

Case B: M^{2}LC With Low-Frequency Mode

Low-frequency mode is necessary whenever a relatively high current with a low frequency on side 2 is required, e.g., in a motor drive with a high start-up torque.

The motor drive application from [19], with a power class similar to Case A, was used for the dimensioning example. The converter output frequency is in the range of 0–50 Hz and the apparent switching frequency is 8 kHz. With five modules per branch, this leads to a mean module switching frequency of 1.6 kHz. The circulating-current inductance $L_{\mathrm{cir}} = 2$ mH, the maximum branch current $i_{\mathrm{b,max}} = 34.4$ A, the maximum side-1 current $i_{1,\mathrm{max}} = 10$ A, and the maximum circulating current $i_{\mathrm{cir,max}} = 10$ A are taken from the paper, as in the previous case.

The dimensioning results for this example, listed in Table IV, indicate that the proposed topology is advantageous only, if the inductor on side 1 is already present from the system (e.g., when the converter is connected to a current dc link of a diode rectifier). The center-tapped inductor topology has just slightly higher dimensioning requirements than the proposed one, while maintaining the same effective inductance on side 1 compared with the standard noncoupled topology.

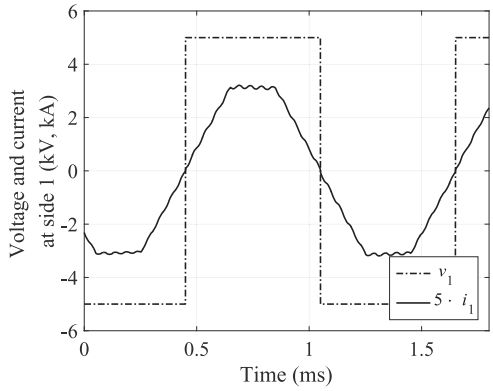

Fig. 6. ACM^{2}LC: voltage and current on side 1.

TABLE V
ACM^{2}LC SIMULATION PARAMETERS

Parameter	Symbol	Value
Frequency on side 1	f_1	833 Hz
Frequency on side 2	f_2	50 Hz
Voltage amplitude on side 1	$\hat{v}_1$	5 kV
Transferred power	P	2 MW
Number of modules	n_{mod}	9
Apparent modulation frequency	f_{m}	20 kHz
Stray inductance of transformer	L_1	330 μH
Load for side 2	L_2, R_2	2 mH, 2 mΩ
	V_2 (l-l)	3.3 kV
Eff. circulating-current inductance	L_{cir}	800 μH
Module capacitor	C_{mod}	2 mF
Module voltage	V_{mod}	730 V

Case C: AC/AC M^{2}LC

AC/AC M^{2}LC (ACM^{2}LC) topology can have similar dimensioning ratings as in Case A or Case B, depending on the application and control approach used. When using relatively low frequencies on both sides (e.g., 16.6 Hz on side 1 and 50 Hz on side 2 for connecting the train link to the grid), the Case A dimensioning is present. If a higher frequency on side 1 (e.g., 500 Hz) is employed in order to minimize the module energy variation, higher circulating currents are required, resulting from a dedicated energy-controlling approach (e.g., the approach presented in [15]). In this case, the dimensioning results are similar to the Case B results.

Side 1 is usually connected to an inductive link or a transformer, which provide sufficient inductance for the input current. Therefore, the proposed topology is the most suitable one. Furthermore, the proposed inductor coupling can result in module savings, especially when a medium-frequency link is present.

In this design scenario, we have chosen a 2 MW ACM^{2}LC connected to an 833 Hz ac link generated by an H-bridge voltage-source IGBT converter. The currents through the converter are controlled to achieve zero-current switching for the H-bridge converter, Fig. 6. Between the H-bridge converter and ACM^{2}LC, a medium-frequency isolating transformer is connected with a stray inductance of 330 μH.

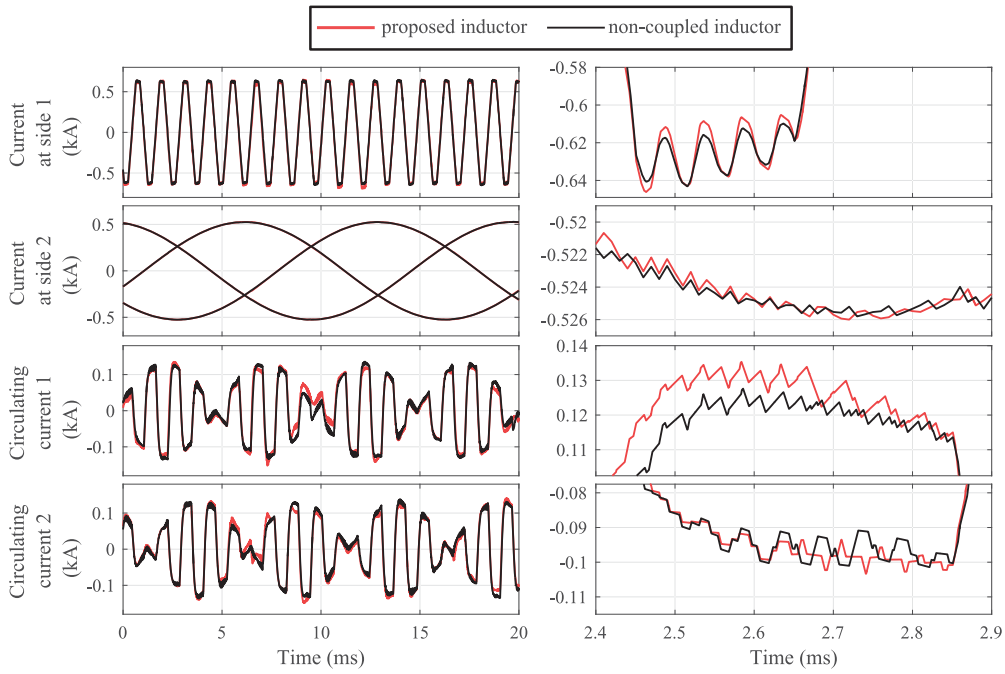

Fig. 7. ACM^{2}LC: simulated currents.

TABLE VI
INDUCTOR DESIGN RESULTS FOR CASE C EXAMPLE

	Noncoupled	Center tapped	Proposed
w	8	5	4
a	12.85 cm	12.65 cm	9.91 cm
b	6.63 cm	5.24 cm	4.69 cm
Δl	3.32 mm	2.51 mm	1.98 mm
R_b	0.48 mΩ	0.28 mΩ	0.18 mΩ
Total copper volume	8.23 ℓ	4.72 ℓ	3.08 ℓ
Total core volume	77.13 ℓ	39.39 ℓ	13.18 ℓ

The ACM^{2}LC was simulated with both noncoupled and proposed inductor topologies using Mathworks Simulink in combination with Plexim Plecs for the power section of the model. The converter parameters are listed in Table V. The approach from [15] was used for the converter control.

From the simulated data (see Fig. 7), the values of the currents needed for the inductor dimensioning can be concluded: The maximum branch current $i_{\mathrm{b,max}} = 660$ A, the maximum side-1 current $i_{1,\mathrm{max}} = 640$ A, and the maximum circulating current $i_{\mathrm{cir,max}} = 150$ A. Besides, the detail on the right side of the figure shows that the current ripple is higher for the current i_1 with the proposed branch inductor. This is because the inductor has no effect on the input current. The ripple at the output current is comparable for both inductor topologies, as the effect of the branch inductor is very small in comparison to the one of inductance value L_2. The circulating-current ripple is almost identical for both inductor couplings, as expected.

In Table VI, the inductor design results for this converter example are listed. Significant savings of conductor and core material are visible for the proposed inductor topology, similarly to Case B.

The mentioned voltage drop v_{Leff} caused by the effective inductance on side 1 can be calculated from the current waveform and the inductance influencing the currents on side 1

$$v_{\mathrm{Leff}} = L_{\mathrm{eff}} \cdot \frac{\Delta i_1}{\Delta t} = L_{\mathrm{eff}} \cdot \frac{\hat{i}_1}{\frac{1}{6 \cdot f_1}} \quad . \tag{19}$$

For the noncoupled (and the center-tapped) inductor topology, the effective inductance consists of the transformer stray inductance (L_1) and the part caused by branch inductors: $L_{\mathrm{eff}} = L_1 + \frac{L_{\mathrm{cir}}}{6}$ (see Table. II). Consequently, the voltage drop across these inductances is 1483 V. On the other hand, for the proposed inductor topology, the effective inductance consists only of stray inductance L_1 (see Table II). Therefore, the resulting voltage drop in this case is only 1056 V. The difference between the voltage drops translates into approximately 200 V less required branch voltage with the proposed topology. As shown in Fig. 8, this can even lead to a lower amount of required modules per branch (in the given example eight instead of nine) with the proposed inductor topology.

VI. LIMITATIONS AND SPECIAL CASES

In this section, an enhanced discussion on the limitations of the proposed inductor topology and behavior in special cases is presented.

A. Core Saturation

All described inductor couplings can be realized with iron cores. Iron-core inductors are favorable because of their lower volume and lower price in comparison to air-core inductors. Nevertheless, the main disadvantage of the iron core is its saturation. If the inductor is used outside of the specified current range, the value of the inductance drops. This leads to an

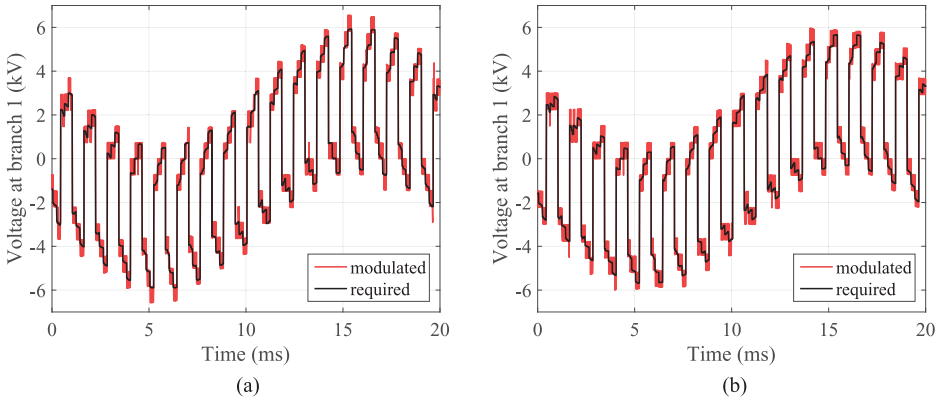

Fig. 8. ACM^{2}LC: simulated branch voltage. (a) Noncoupled branch inductors. (b) Proposed coupling.

TABLE VII
INFLUENCE OF AN IMPRECISELY SET RELUCTANCE ON THE CONVERTER EQUATIONS

$$\mathbf{A}_\mathrm{P} = \begin{bmatrix} -\frac{3R_1+2R_\mathrm{b}}{3L_1} & 0 & 0 & 0 & 0 \\ 0 & -\frac{2R_2+R_\mathrm{b}}{2L_2} & 0 & 0 & 0 \\ 0 & 0 & -\frac{2R_2+R_\mathrm{b}}{2L_2} & 0 & 0 \\ 0 & 0 & 0 & -\frac{61}{180}\frac{R_\mathrm{b}}{L_\mathrm{b}} & \frac{1}{180}\frac{R_\mathrm{b}}{L_\mathrm{b}} \\ 0 & 0 & 0 & \frac{1}{180}\frac{R_\mathrm{b}}{L_\mathrm{b}} & -\frac{61}{180}\frac{R_\mathrm{b}}{L_\mathrm{b}} \end{bmatrix}, \mathbf{E}_\mathrm{P} = \begin{bmatrix} \frac{1}{L_1} & 0 & 0 & 0 \\ 0 & -\frac{1}{L_2} & 0 & 0 \\ 0 & 0 & -\frac{1}{L_2} & 0 \\ 0 & 0 & 0 & 0 \\ 0 & 0 & 0 & 0 \end{bmatrix},$$

$$\mathbf{B}_\mathrm{P} = \begin{bmatrix} -\frac{1}{3L_1} & -\frac{1}{3L_1} & -\frac{1}{3L_1} & -\frac{1}{3L_1} & -\frac{1}{3L_1} & -\frac{1}{3L_1} \\ -\frac{1}{3L_2} & \frac{1}{3L_2} & \frac{1}{6L_2} & -\frac{1}{6L_2} & \frac{1}{6L_2} & -\frac{1}{6L_2} \\ 0 & 0 & -\frac{\sqrt{3}}{6L_2} & \frac{\sqrt{3}}{6L_2} & \frac{\sqrt{3}}{6L_2} & -\frac{\sqrt{3}}{6L_2} \\ -\frac{61}{720L_\mathrm{b}} & -\frac{61}{720L_\mathrm{b}} & \frac{62}{720L_\mathrm{b}} & \frac{62}{720L_\mathrm{b}} & -\frac{1}{720L_\mathrm{b}} & -\frac{1}{720L_\mathrm{b}} \\ \frac{1}{720L_\mathrm{b}} & \frac{1}{720L_\mathrm{b}} & -\frac{62}{720L_\mathrm{b}} & -\frac{62}{720L_\mathrm{b}} & \frac{61}{720L_\mathrm{b}} & \frac{61}{720L_\mathrm{b}} \end{bmatrix}.$$

unintentionally rising current. To avoid this effect, a reasonable reserve must be chosen for the specified current range, or a noncoupled air-core inductor must be used.

In high-voltage direct current (HVDC) applications, nonsaturable inductors are necessary, as these are also needed for handling faults at the dc side of the converter. Therefore, the center-tapped and proposed inductors are rather unsuitable. On the other hand, for smaller converters working at medium-voltage range, where converters are connected directly to the link of a back-to-back converter (or isolating medium-frequency transformer with ACM^{2}LC), the fault handling on side 1 is not a crucial issue. In this case, the use of iron-core inductors offers a significant cost advantage.

B. Parasitic Effects

Each inductor winding has a parasitic leakage inductance and a parasitic coupling through the air. Nevertheless, the coupling through the air is very weak, as the windings are positioned relatively far away from each other. As known from the standard inductors in power electronics, the size of this leakage inductance is expected to be in the range of a few percent of the target inductance. For the dynamic behavior, this part can be modeled as a series-connected inductor for every branch, and it behaves as a noncoupled inductor from Table II. The magnetic flux generated by the branch current through the leakage inductance can also add to the total magnetic flux causing the saturation in the magnetic core. Nevertheless, because of the small value of the leakage inductance, these effects are negligible.

Additionally, different inductor asymmetries are created during the inductor construction process. In general, these asymmetries cause cross couplings, and thus, change the behavior of the system. The strength of the cross couplings is directly proportional to the amount of asymmetry, therefore, these should be avoided. In Table VII, the influence of an asymmetry caused by imprecisely set reluctance is shown. In this case, the reluctance value of the middle core leg is five percent higher than the reluctances of the other two legs. This leads to a weak cross coupling between the circulating currents, as visible from matrix $\mathbf{A}_\mathrm{P}$. The input and output currents are in this case uninfluenced.

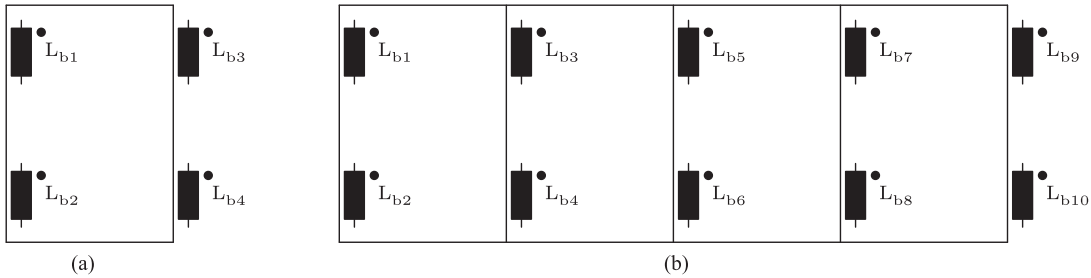

Fig. 9. Application to other than three-phase M^{2}LC. (a) Two-leg M^{2}LC (four branches). (b) Five-leg M^{2}LC (10 branches).

C. Unbalanced System on Side 2

In general, the function of the proposed inductor is not restricted by an unbalanced ac system connected to side 2, as the instantaneous value of the side-2 current is still split symmetrically between the upper and lower branch. Nevertheless, different current (or voltage) amplitudes at different converter phases might cause different mean output-phase powers $P_{2,\mathrm{A}}$, $P_{2,\mathrm{B}}$, $P_{2,\mathrm{C}}$, causing steady-state circulating current terms (at the frequency of the system connected to side 1).

The maximum effective value of circulating current $I_{\mathrm{cir,max}}$ can be determined from the power balance equation by knowing the maximum mean power difference $\Delta P_{2,\mathrm{max}}$ between two output phases

$$I_{\mathrm{cir,max}} = \frac{1}{2} \cdot \frac{\Delta P_{2,\mathrm{max}}}{V_1} \quad . \tag{20}$$

Consequently, these additional circulating current terms must be considered in the design of the coupled inductor.

D. Application to n-Leg M^{2}LC

The proposed inductor topology is generally transferable to other M^{2}LC topologies with a different number of legs (phases). In Fig. 9, the coupled inductors for two-leg (single-phase) and five-leg (five-phase) M^{2}LC are displayed; the converter topologies can be derived by altering the number of converter legs regarding the three-leg converter in Fig. 2(a).

The idea here is the very same as for the standard three-phase M^{2}LC: The output ac current is split symmetrically between the upper and lower branch. Because of the inductor directions, the sum of the magnetic fluxes caused by the output current is zero in each leg. Per definition, the input current splits symmetrically between the converter legs. According to the law of superposition, the resulting flux in particular inductors is zero (there is no path for the input current components). Therefore, the inductor applies to the internal circulating currents only.

VII. Experimental Verification

The general functionality and the properties of the proposed topology are verified on a down-scaled converter prototype. The test setup shows the proper functionality of the topology and its influence on the current ripple in the case of dc/ac M^{2}LC operation. An induction machine with a fixed rotor was used as

TABLE VIII
Laboratory Setup Parameters

Parameter	Symbol	Value
Frequency on side 1	f_1	0 Hz (dc)
Frequency on side 2	f_2	50 Hz
Direct voltage on side 1	V_1	24 V
Current amplitude on side 2	$\hat{i}_2$	3.57 A
Number of modules	n_{mod}	3
Apparent modulation frequency	f_{m}	10 kHz
Inductor on side 1	L_1	310 μH
Load for side 2	L_2, R_2	11.9 mH, 2.9 Ω
	V_2	0 V
Eff. circulating-current inductance	L_{cir}	960 μH
Module capacitor	C_{mod}	20.21 mF
Module voltage	V_{mod}	14 V

Fig. 10. Proposed inductor prototype; dimension of core: 80 × 82 mm.

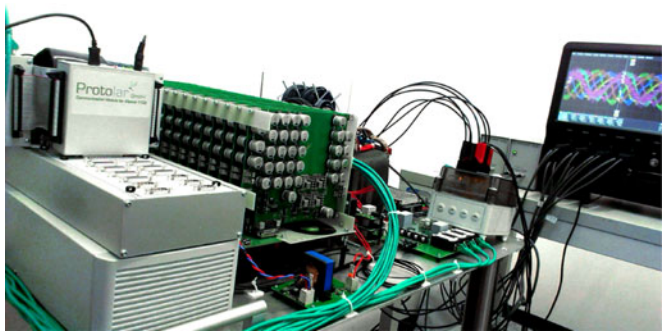

Fig. 11. Laboratory setup.

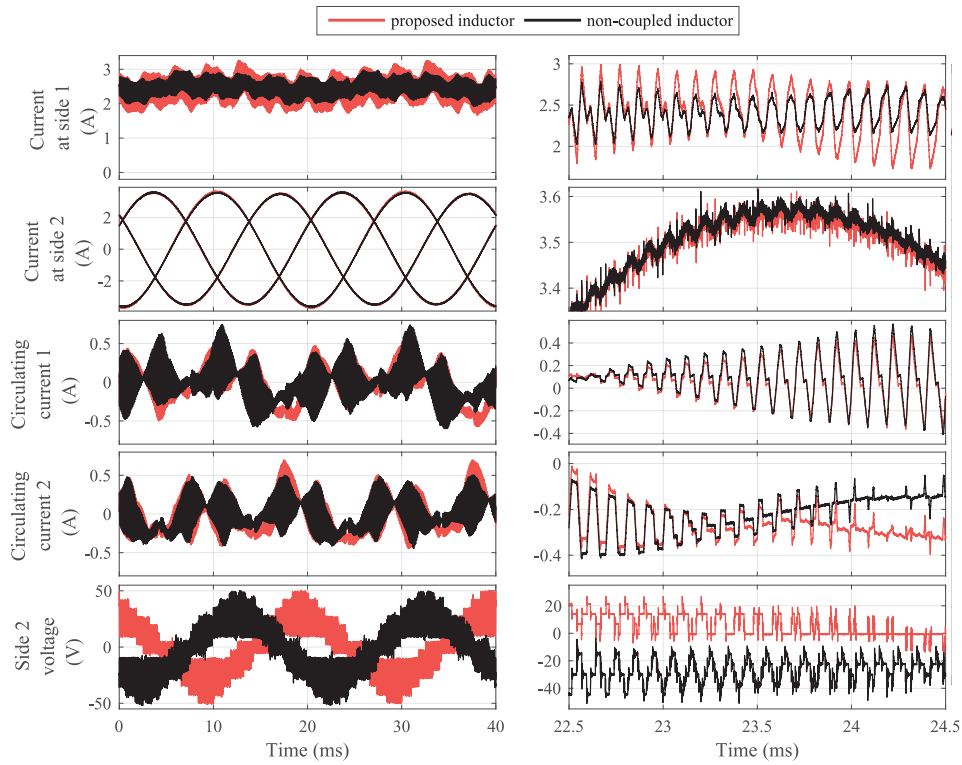

Fig. 12. M^{2}LC-measured data.

a passive load for the converter. The setup parameters are listed in Table VIII.

The proposed inductor (see Fig. 10) was built with a strip wound core with an air gap. The effective circulating current inductance was set quite precisely (measured: $L_{\mathrm{cir},1} = L_{\mathrm{cir},2} =$ 1 mH). The inductance applied to the current on side 1 was measured as 17 μH. The effective side-2 inductance is 6 μH. The calculated circulating current maximum derived from the core saturation constraint is at 10 A. However, the branch current is limited thermally to approximately 9 A by the inductor winding wire. The inductor prototype, similarly to the converter prototype, is not optimized. Their main purpose is to prove the functionality of the proposed inductor coupling.

The laboratory setup comprises 18 H-bridge modules (three modules per branch), Fig. 11. The converter prototype already includes noncoupled air-core inductors, with an effective circulating-current inductance equal to the one of the coupled inductor prototype (branch inductance $L_{\mathrm{b}} = 240$ μH). These were then replaced with the proposed coupled inductor for the measurement comparison. Note, that the installed module capacitance is higher than necessary. Nevertheless, this does not influence the size of the circulating currents significantly because a decoupled current control was used. The control of the converter is provided with a dSpace control system in combination with the Protolar FPGA.Comm logic expansion box, enabling the communication with analog-to-digital converters and the modules. The measured data were obtained with an eight-channel oscilloscope with six current probes and one differential voltage probe.

In Fig. 12, the traces measured with an oscilloscope are plotted showing the particular currents and line-to-line voltages on side 2. The voltages were measured between different clamps of the machine for the different topology scenarios to obtain a better visibility of the curves. The voltages prove the multilevel character of the converter. The plotted currents are zoomed in to show the current ripple. Looking at the circulating currents, the similarity of the ripple for both inductor topologies can be seen. This verifies that the inductors were designed correctly to have the same value of the inductance applied to the circulating current. The amplitudes of the circulating currents compensate for the power imbalance caused by a slight load asymmetry. The current ripple of the side-1 current for the proposed topology is observably higher due to the excluded influence of this inductor on this side. The theoretical findings imply that the ripple on side 2 should also be higher. This is not visible, though, because the load inductor value is significantly higher than the influence of the branch inductors.

VIII. Conclusion

This paper proposed a novel branch-inductor coupling for M^{2}LC, which was then compared with the standard noncoupled topology and the topology with center-tapped inductors on the basis of the respective equation systems and dimensioning examples. The operation of the proposed inductor coupling was verified by simulation and an experiment.

The proposed coupling shows significant savings of inductor material in comparison to the other topologies for applications providing enough inductance on both the input and output side of the converter, as the coupled branch inductors do not affect them. However, for applications without sufficient input inductance and with an input current, which is not significantly higher than

the circulating currents, the center-tapped inductor topology shows a better performance.

The proposed inductor topology is rather unsuitable for HVDC applications, where air-core inductors are needed for dc side fault handling. Nevertheless, a significant improvement for ac/ac M^2LC with medium-frequency input link is possible, as the value of the effective input inductance is crucial for the voltage drop in case of single-phase medium-frequency ac input, and a sufficient inductance value is obtained from the isolating-transformer stray inductance. This results in a smaller inductor design and a different dimensioning of the required maximum branch voltage. For these reasons, it is beneficial to use the proposed coupled inductor topology.

REFERENCES

[1] J. Kucka, D. Karwatzki, L. Baruschka, and A. Mertens, "Improved modular multilevel converter topology with magnetically coupled branch inductors," in *Proc. IEEE Energy Convers Congr. Expo.*, Sep. 2015, pp. 3593–3600.

[2] P. Hammond, "A new approach to enhance power quality for medium voltage AC drives," *IEEE Trans. Ind. Appl.*, vol. 33, no. 1, pp. 202–208, Jan./Feb. 1997.

[3] R. Marquardt, A. Lesnicar, and J. Hildinger, "Modulares Stromrichterkonzept für Netzkupplungsanwendungen bei hohen Spannungen," *ETG-Fachtagung, Bad Nauheim*, 2002.

[4] C. Oates, "A methodology for developing chainlink converters," in *Proc. 13th Eur. Conf. Power Electron. Appl.*, 2009, pp. 1–10.

[5] L. Baruschka and A. Mertens, "A new three-phase AC/AC modular multilevel converter with six branches in hexagonal configuration," *IEEE Trans. Ind. Appl.*, vol. 49, no. 3, pp. 1400–1410, May 2013.

[6] F. Kammerer, J. Kolb, and M. Braun, "Optimization of the passive components of the modular multilevel matrix converter for drive applications," in *Proc. PCIM Europe*, 2012, pp. 583–590.

[7] W. Kawamura, M. Hagiwara, and H. Akagi, "Design and evaluation of AC inductors indispensable to a modular multilevel cascade converter (MMCC-TSBC) for medium-voltage motor drives," in *Proc. IEEE 2nd Int. Future Energy Electron. Conf.*, Nov. 2015, pp. 1–6.

[8] D. Karwatzki, L. Baruschka, J. Kucka, M. von Hofen, and A. Mertens, "Improved Hexverter topology with magnetically coupled branch inductors," in *Proc. 16th Eur. Conf. Power Electron. Appl.*, Aug. 2014, pp. 1–10.

[9] M. Hagiwara, R. Maeda, and H. Akagi, "Negative-sequence reactive-power control by the modular multilevel cascade converter based on double-star chopper-cells (MMCC-DSCC)," in *Proc. IEEE Energy Convers. Congr. Expo.*, Sep. 2010, pp. 3949–3954.

[10] X. Shi, Z. Wang, L. Tolbert, and F. Wang, "Modular multilevel converters with integrated arm inductors for high quality current waveforms," in *Proc. IEEE ECCE Asia Downunder*, Jun. 2013, pp. 636–642.

[11] A. Korn, M. Winkelnkemper, and P. Steimer, "Low output frequency operation of the modular multi-level converter," in *Proc. Energy Convers. Congr. Expo.*, Sep. 2010, pp. 3993–3997.

[12] M. Glinka and R. Marquardt, "A new AC/AC multilevel converter family," *IEEE Trans. Ind. Electron.*, vol. 52, no. 3, pp. 662–669, Jun. 2005.

[13] M. Schnarrenberger, F. Kammerer, M. Gommeringer, J. Kolb, and M. Braun, "Current control and energy balancing of a square-wave powered 1AC-3AC modular multilevel converter," in *Proc. IEEE Energy Convers. Congr. Expo.*, Sep. 2015, pp. 3607–3614.

[14] Y. Okazaki, M. Hagiwara, and H. Akagi, "Multiple medium-voltage motor drives using modular multilevel cascade converters with medium-frequency transformers," in *Proc. IEEE 2nd Int. Future Energy Electron. Conf.*, Nov. 2015, pp. 1–6.

[15] J. Kucka and L. Baruschka, "A hybrid modular multilevel DC/AC converter," in *Proc. 17th Eur. Conf. Power Electron. Appl.*, Sep. 2015, pp. 1–10.

[16] D. Karwatzki, M. Dokus, L. Baruschka, J. Kucka, and A. Mertens, "Branch energy balancing with a generalised control concept for modular multilevel topologies using the example of the modular multilevel converter," in *Proc. 18th Eur. Conf. Power Electron. Appl.*, Sep. 2016, pp. 1–10.

[17] Y. Wan, S. Liu, and J. Jiang, "Generalised analytical methods and current-energy control design for modular multilevel cascade converter," *IET Power Electron.*, vol. 6, no. 3, pp. 495–504, Mar. 2013.

[18] N. Thitichaiworakorn, M. Hagiwara, and H. Akagi, "Experimental verification of a modular multilevel cascade inverter based on double-star bridge cells," *IEEE Trans. Ind. Appl.*, vol. 50, no. 1, pp. 509–519, Jan. 2014.

[19] J. Kolb, F. Kammerer, and M. Braun, "Dimensioning and design of a modular multilevel converter for drive applications," in *Proc. 15th Int. Power Electron. Motion Control Conf.*, Sep. 2012, pp. LS1a–1.1–1–LS1a–1.1–8.

Jakub Kucka (S'15) received the Ing. degree in electrical engineering from Czech Technical University in Prague, Prague, Czech Republic, in 2014. Since 2014, he has been working toward the Ph.D. degree in electrical engineering from the Institute for Drive Systems and Power Electronics, Leibniz Universität Hannover, Hanover, Germany.

His research interests include modular multilevel converters, their control and design, and control approaches for minimizing the installed module capacitance.

Dennis Karwatzki (S'13) received the Dipl.-Ing. degree in electrical engineering from the University of Kaiserslautern, Kaiserslautern, Germany, in 2012. Since 2012, he has been working toward the Ph.D. degree in electrical engineering from the Institute for Drive Systems and Power Electronics, Leibniz Universität Hannover, Hanover, Germany.

His main research interests include modular multilevel converters and their control.

Lennart Baruschka (M'14) received the Diploma and Ph.D. degrees in electrical engineering from Leibniz Universität Hannover, Hanover, Germany, in 2008 and 2013, respectively.

While finishing his thesis on the modular multilevel converter "Hexverter," which he invented and investigated, he founded Protolar, a company dedicated to the quick realization of power electronic prototypes. Among prototyping, testing and characterization of power converters, Protolar also develops and offers tools to help other researchers with power electronic prototyping.

Axel Mertens (S'89–M'92) received the Dipl.-Ing. and Dr.-Ing. (Ph.D.) degrees in electrical engineering from Rheinisch-Westfaelische Technische Hochschule Aachen University, Aachen, Germany, in 1987 and 1992, respectively.

In 1989, he was a Research Associate in the Wisconsin Electric Machines and Power Electronics Consortium, University of Wisconsin, Madison, WI, USA. From 1993 to 2004, he was with Siemens Drive Technologies, Germany, where he was responsible for the control of large drives ranging from three-level high-voltage insulated-gate bipolar transistor inverters to cycloconverters and load-commutated inverters. In 2004, he was appointed the Professor of power electronics and drives at Leibniz Universität Hannover, Hanover, Germany. Since 2012, he has been the Head of the Department Converter Technology, Fraunhofer Institute for Wind Energy and Energy System Technology. His research interests include application of wide bandgap semiconductors, condition monitoring of power semiconductor devices, design of power electronic circuits, modular multilevel converters, and control of electronic power converters and drives. His preferred fields of application are industrial drives, electric vehicles, and grid-connected inverters such as in wind power systems. He published more than 100 technical papers and holds a number of patents.

Prof. Mertens is an Associate Editor of the IEEE TRANSACTIONS ON POWER ELECTRONICS and served as the Chairman of the IEEE Joint German Chapter of the IEEE Industry Applications, IEEE Power Electronics, and IEEE Industrial Electronics Societies.